Journal of Power Sources 269 (2014) 994–999

Contents lists available at ScienceDirect

Journal of Power Sources

journal homepage: www.elsevier.com/locate/jpowsour

Short communication

X-ray absorption fine structure imaging of inhomogeneous electrode reaction in $LiFePO_4$ lithium-ion battery cathode

Misaki Katayama [a], Koichi Sumiwaka [a], Ryota Miyahara [a], Hisao Yamashige [b], Hajime Arai [b], Yoshiharu Uchimoto [c], Toshiaki Ohta [d], Yasuhiro Inada [a,*], Zempachi Ogumi [b]

[a] Department of Applied Chemistry, Ritsumeikan University, Kusatsu 525-8577, Japan
[b] Office of Society-Academia Collaboration for Innovation, Kyoto University, Uji 611-0011, Japan
[c] Graduate School of Human and Environmental Studies, Kyoto University, Kyoto 606-8501, Japan
[d] Research Organization of Science and Engineering, Ritsumeikan University, Kusatsu 525-8577, Japan

ARTICLE INFO

Article history:
Received 16 December 2013
Accepted 17 March 2014
Available online 13 April 2014

Keywords:
Chemical state map
XAFS imaging
Reaction distribution
Reaction channel

ABSTRACT

To improve the performance of rechargeable lithium-ion batteries, a microscopic understanding of the electrochemical reaction at the cathode is necessary. The spatial distribution of the electrode redox reaction for the $LiFePO_4$ cathode was analyzed by X-ray absorption fine structure (XAFS) imaging. Chemical state maps of the planar cathode electrode obtained by the *in situ* XAFS imaging revealed the inhomogeneity of the chemical state of Fe during the charge/discharge process. The chemical state maps for the reverse charge/discharge process demonstrated the reversibility of the inhomogeneous distribution. The in-plane radial progress of the reaction distribution strongly suggests that the inhomogeneous electrode reaction is caused by the difference in electrical conductivity; the charging and discharging reactions proceed through reaction channels with low electrical resistance in the cathode.

1. Introduction

Lithium-ion secondary batteries (LIBs) are widely used as energy sources for portable devices. Recently, the demand for high-performance LIBs has increased for applications such as electric vehicles and storage devices. The present requirements for LIBs are high energy density, good cycle performance, and safety in various environments. Materials for the cathode and anode have been the focus of research and development to improve LIB performance. Phosphates and silicates are promising candidates for high-capacity cathode materials [1–6], and carbon, silicon, and their composites have been investigated extensively as anode materials [7–10]. However, mechanistic studies of the chemical reactions at the electrodes are important for understanding and overcoming the current limitations of LIBs and thus promoting a low-carbon society that has a smaller environmental impact.

Lithium iron phosphate ($LiFePO_4$; LFP) is a promising compound for LIB cathodes. Padhi et al. [11] highlighted its advantages: abundance, low cost, and stability of its olivine crystal structure. Malik et al. [12] published a comprehensive review of the LFP cathode and summarized the Li^+ ion insertion mechanisms. The similar lattice structures of LFP and $FePO_4$ (FP) contribute to the quantitative electrode reaction, meaning the Li^+ ions are used effectively. In LFP, all the Li^+ ions can be involved in the electrode reaction, whereas in $LiCoO_2$ excessive delithiation can cause structural collapse [13]. However, owing to their low electrical conductivity, it is necessary to coat the LFP particles with carbon as a conductive material [14,15]. The size and surface structure of the LFP particle also affect battery performance [4]. LFP has been synthesized by using many conventional techniques, such as the solid-state, hydrothermal, and sol–gel methods [11,16–18], as reviewed by Jugović et al. [19]. Flame spray pyrolysis and the use of a virus to synthesize amorphous $FePO_4$ nanowires have also been reported as synthetic methods [20,21]. LFP electrodes with porous, hollow spherical, and high-density structures have been used to examine the effect of morphology on electrode performance [22–24]. Various Fe precursors have been examined for morphology-controlled synthesis [25]. There are also many studies of carbon sources and additional compounds for improving LIB performance [25–31].

A mechanistic understanding of electrochemical reactions in the LIB cathode is also important for improving LIB performance. The reactions that occur at the cathode are complicated because they consist of many physicochemical processes, such as Li^+ ion

* Corresponding author. Tel.: +81 77 561 2781; fax: +81 77 561 2659.
E-mail address: yinada@fc.ritsumei.ac.jp (Y. Inada).

http://dx.doi.org/10.1016/j.jpowsour.2014.03.066
0378-7753/

insertion/dissociation, redox reactions of the metal species, and structural changes in the host crystal. Recently, an *in situ* X-ray diffraction study of the mechanism of the redox reaction between the LFP and FP particles was published [32]. In that study, the short-lived metastable state compensated for the structural mismatch between the LFP and FP particles. In addition to this type of microscopic study, spatial observations of larger electrodes are required to link the atomic-scale mechanism to the actual LIB performance. This is because the cathode is generally manufactured as a mixture of an active material, a conductive additive, and a polymer binder to increase the conductivity of both the lithium ions and electrons in the electrode by increasing the surface area of component particles. Although many studies have been performed to identify effective conductive additives, the optimal mixing ratio for the binder material, and the electrode thickness [33–37], the crucial factor for the electrode that determine the LIB performance under operating conditions are still unclear. X-Ray absorption fine structure (XAFS) is the best technique for determining the chemical state of transition metal species. Chemical state mapping of the LFP cathode by X-ray diffraction has been reported [38,39], and Ouvrard et al. [40] have recently reported the reaction distribution of the LFP cathode with synchrotron XAFS techniques. They hypothesized that the observed heterogeneous behavior is related to the quality of grain connectivity to ionic and electronic percolating networks. We have recently developed the XAFS imaging technique for the spatial analysis of the oxidation state of transition metal species in planar battery electrodes [41]. In this study, we present the inhomogeneous reaction distribution for the LFP cathode during operation and discuss the origin of the inhomogeneous charge/discharge process. We examine the reaction distribution of LFP cathode by *in situ* XAFS imaging with a 2-dimensional detector and discuss the dynamic behavior of the electrode reactions on the basis of these results.

2. Experimental

The XAFS imaging measurements were performed at the BL-4 beamline of the SR Center (Ritsumeikan University, Japan) and at the NW2A beamline of PF-AR (High Energy Accelerator Research Organization, Japan). Details of the measurement system have previously been described in the literature [41]. The transmitted X-ray images were collected by using a 2-dimensional detector. The images were converted to XAFS spectra by scanning the incident X-ray energy at each detector pixel with a spatial resolution of $10 \times 10\ \mu m^2$. The energy shift caused by the vertical divergence of the X-ray beam on the monochromator surface was corrected by a geometrical correction factor [41]. The chemical state map was produced from the absorption edge energy (E_0) and the absorbance difference ($\Delta\mu t$) between the pre- and post-edge region by analyzing the X-ray absorption near edge structure (XANES). The E_0 value was defined as the X-ray energy at the local maximum of the first derivative of the XANES spectrum. The chemical state mapping was derived from the E_0 shift in response to the oxidation state of the absorbing atoms. It should be noted that all species in the X-ray path are accumulated in the XANES spectrum and thus their chemical states are averaged in the direction of the X-ray, which is perpendicular to the cathode sheet.

The cathode was prepared by mixing carbon coated LFP powder, acetylene black, and polyvinylidene difluoride at a weight ratio of 8:1:1. The slurry mixture was spread on an aluminum foil to a thickness of 100 μm, dried at 353 K, and then pressed. A current collector tab was ultrasonically welded to the cathode sheet. The LIB cell was assembled from the cathode sheet (15×25 mm), Li foil as the anode, separator sheets, and 1 mol dm^{-3} $LiPF_6$ solution in a 3:7 (v/v) mixture of ethylene carbonate and ethyl methyl carbonate. An aluminum-coated laminate envelope was used as the outer shell of the battery cell. The assembled cell was aged by three charge/discharge cycles, and the capacity was determined during the discharge process. The cell voltage was restricted to 2.5–4.2 V (*vs.* Li^+/Li). A typical charge/discharge profile is shown in Supplementary Fig. S1.

3. Results and discussion

3.1. Reaction distribution of LFP cathode

Three cells were charged to 0%, 25%, or 50% *versus* their discharge capacity and disassembled under inert atmosphere. The cathode was washed with dimethyl carbonate and dried to prevent further Li^+ diffusion. Fig. 1 shows the chemical state maps generated based on the oxidation state of Fe. The cathode sheets were set perpendicular to the X-ray beam, and Fig. 1 shows the in-plane distribution of Fe species on the cathode sheet. The blue (in the web version) pixels correspond to Fe(II) in LFP, and the red pixels are Fe(III) in delithiated FP. The XANES spectra are shown in Fig. 1(a) and agree with those measured independently. Yellow pixels indicate a mixture of Fe(II) and Fe(III), and the sum of LFP and FP reproduces the XANES spectrum well. This additivity is consistent with a previous *in situ* XRD study [32], because the lifetime of the metastable state is too short to detect with present XAFS imaging techniques. The E_0 values (7715 and 7719 eV) used to distinguish the Fe(II) and Fe(III) states were determined from fully charged and discharged cathodes. The difference of 4 eV is in agreement with the value observed when using conventional XAFS [42] and is similar to the difference in E_0 (5 eV) between FeO and Fe_2O_3.

Rounded interconnected spots of Fe(III), with diameters from 200 to 500 μm are observed during the charging process, as shown in Fig. 1(c) and (d). The ratio of the areas of the blue and red pixels is close to the state of charge. The particle radius of the component materials is less than 1 μm, and the cathode surface is uniform at a scale of 10 μm, according to the scanning electron microscopy (SEM) measurements (Supplementary Fig. S2). The homogeneous distribution of Fe species is also supported by the spatial variation of the X-ray absorbance at the Fe K edge (Fig. 2). The E_0 values change across the reaction spot, whereas the values of $\Delta\mu t$ are almost constant. The obtained maps clearly indicate that the oxidation of LFP proceeds heterogeneously in preferential reaction channels. Thus, the speckled pattern implies that the resistance to electron and Li^+ migration is different at different positions in the cathode sheet, as reported by Ouvrard et al. [40].

The *in-situ* experiments revealed the dynamic changeover of the inhomogeneous reaction distribution during the charging process. Chemical state maps at states of charge of 0%, 10%, 20%, 30%, 40%, and 50% are shown in Fig. 1(e). The speckled pattern is also visible, similar to the results of the *ex situ* experiments (Fig. 1(c) and (d)). Some small spots corresponded to Fe(III) appeared during the initial stages of the charging process, and the radial expansion in response to the charging depth also suggests the existence of channels for the electrode reaction.

Chemical state mapping for the LFP cathode has been reported by Liu et al. [38] from microbeam X-ray diffraction. Their results show that a highly charged state is present close to the current collector tab. In this study, there was no evidence that the reaction distribution is related to the position of the current collector tab. The XAFS observations of all the Fe species in both crystalline and amorphous phases may indicate the reason for the difference. XAFS imaging without sample scanning can produce simultaneous measurements for all positions, which is important for determining the extent of the charge/discharge.

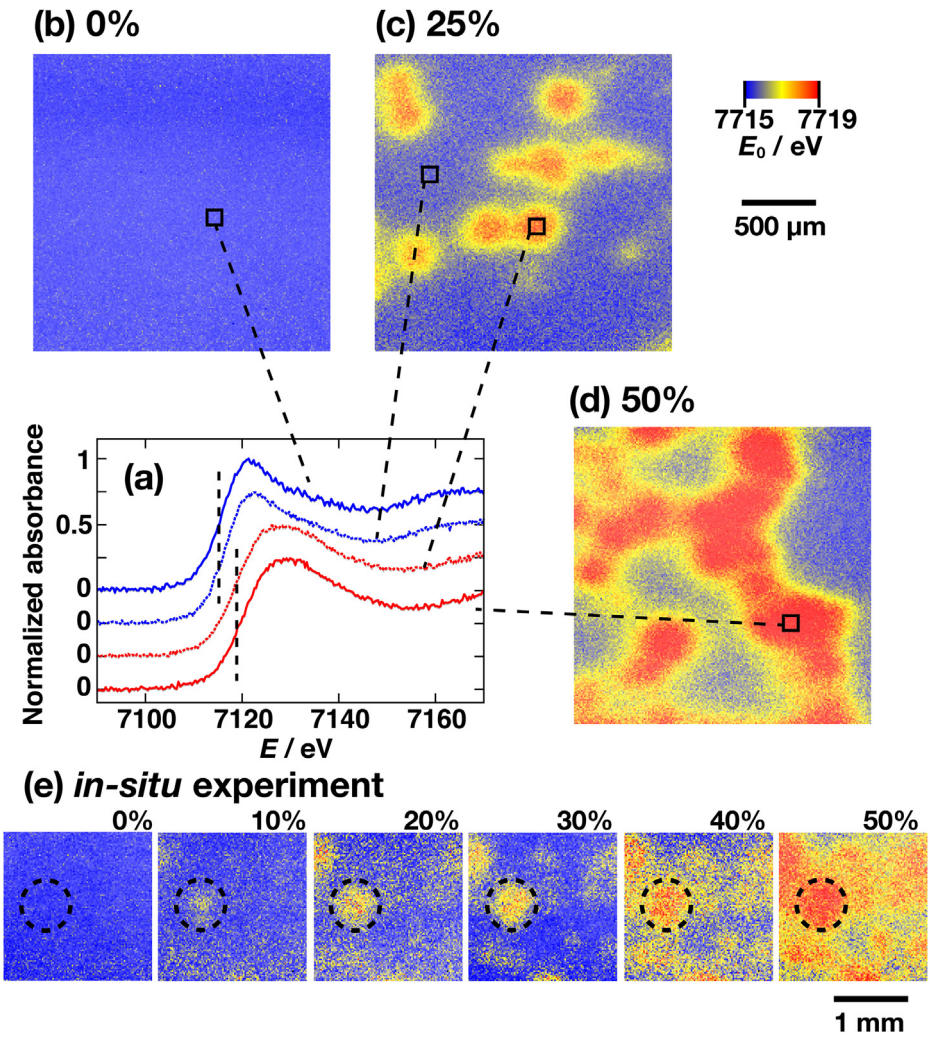

Fig. 1. (a) XANES spectra and (b–d) chemical state maps for the $LiFePO_4$ cathode during charging obtained by *ex situ* XAFS imaging measurements. The successive maps obtained by *in situ* XAFS imaging are shown in (e).

3.2. Reaction distribution during charge/discharge cycles

Fig. 3 shows the chemical state maps for the *in situ* measurements of two successive charge/discharge cycles. The oxidation state of Fe is uniform for the fully charged/discharged cathode (Fig. 3(a) and (b)). The *in situ* measurements reveal that the chemical state map during the middle stage of the discharge process (Fig. 3(d)) is the reverse of that during charging (Fig. 3(c)). Therefore, the electrode reaction starts at the same channel during both the charge and discharge processes, and the redox reactions of the Fe species occur reversibly. In addition, the chemical state maps during the second cycle (Fig. 3(e) and (f)) are very similar to those during the first cycle (Fig. 3(c) and (d)). The spatial distribution of the reaction channels is maintained during repeated charge/discharge cycles, although a uniform distribution appears in the fully charged/discharged state. We observed the reproducibility and reversibility of the inhomogeneous electrode reaction for the first time in this study by using the *in situ* XAFS imaging technique.

The inhomogeneous distribution observed in this study is attributed to the spatial difference in the electrical resistance, which depend on the mobility of electrons and Li^+ ions. Higher mobility corresponds to lower electrical resistance. Positions in the cathode sheet where the resistance is low become reaction channels at which the electrode reaction occurs preferentially.

3.3. Origin of reaction distribution

Electrical resistance is produced at the interfaces between the particles of the conductive additive (carbon) and between the additive and the active material particles. Because the electrical conductivity of LFP is very low (10^{-9}–10^{-10} S cm^{-1}) [43], the LFP particles are homogeneously coated with conductive carbon. The electrical resistance between the LFP and carbon is almost the same for all LFP particles with radii less than 1 μm, so that the electrical resistance at the interface does not contribute to the reaction distribution at the hundred micrometer to millimeter scale. In addition, the Li^+ diffusion between the electrolyte and the active material can contribute to ionic resistance, and the ionic conductivity may not produce a large-scale reaction distribution because of the much smaller particle size of LFP.

Resistance to electron and Li^+ migration also exists in LFP particles. The migration mechanisms for the charge/discharge reaction in a single LFP particle have been reported [11,32,44–48]. The LFP and FP phases are thought to coexist in the particles, and the phase transition can be expressed in terms of the domino cascade model

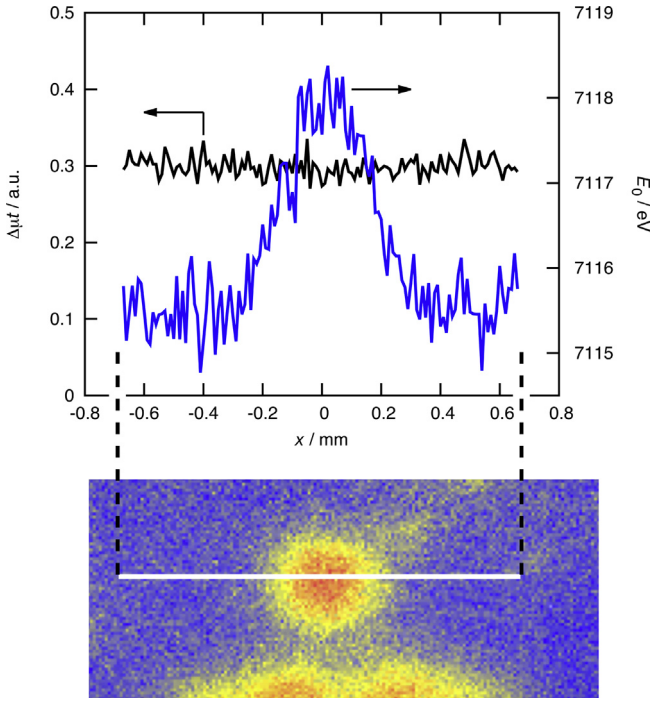

Fig. 2. Values of $\Delta\mu t$ and E_0 across the selected reaction spot.

[47]. Recently, a metastable phase was demonstrated by time-resolved X-ray diffraction [32,49]; however, this short-lived species was not detected by the XAFS imaging method for equilibrated states. Because particles with different resistances are randomly distributed over the cathode sheet, the resistance variation of the LFP particles cannot explain the radial progress of the electrode reaction at the reaction channel.

The cathode mixture, composed of the active material and conductive additive, is filled with the electrolyte solution. The solid-phase ratio in the cathode mixture is estimated to be about 35%, on the basis of electrode density and the thickness. Thus, Li^+ ion diffusion is considered to be homogeneous in the spongy cathode mixture and does not explain the reaction distribution and its radial expansion. The electrons move through the conductive particles and carbon coating and come into contact with the active material with the current collector. Therefore, the pathways with low electrical resistance are different at different positions in the cathode sheet, depending on the filling pattern of the LFP particles with low conductivity. The tree-like development of these electron pathways can explain the radial expansion of the inhomogeneous distribution. Therefore, these pathways form the reaction channel, which is the origin of the inhomogeneous reaction distribution observed in this study. The electron pathways are maintained during the charge/discharge cycles because the solid particles are stationary, which explains the reversibility and the reproducibility of the inhomogeneous distribution.

Ouvrard et al. have reported the reaction distribution originating from the pressure difference in the battery cell [40]. The physical contact between cathode particles is increased by pressure on the electrode. This can be explained by the spatial difference in the electronic conductivity. In contrast, the Al-laminated bag cell used in this study was kept at a constant pressure over the cathode sheet. The radial distribution shown in Fig. 1 is not caused by a difference in the confining pressures.

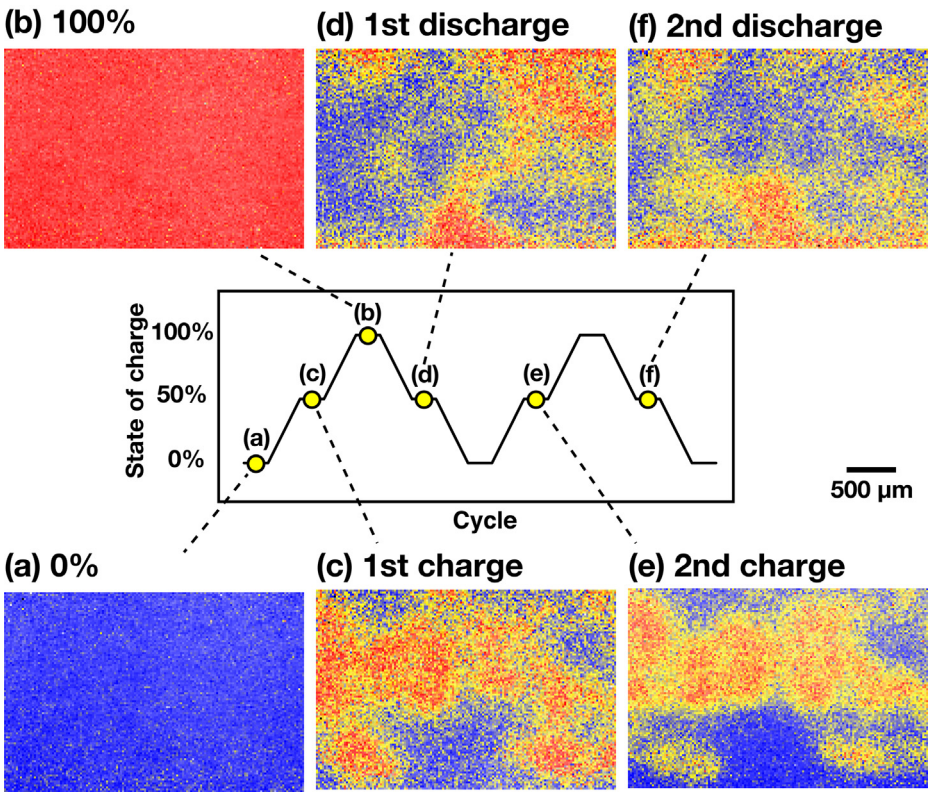

Fig. 3. Chemical state maps for the *in situ* XAFS imaging measurements during two successive charge/discharge cycles. The first charge process is from (a) to (b) *via* (c), at which the state of charge is 50% *versus* the discharge capacity. The map in (d) is at a state of charge of 50% during the first discharge process. The corresponding maps for the second cycle are given in (e) and (f).

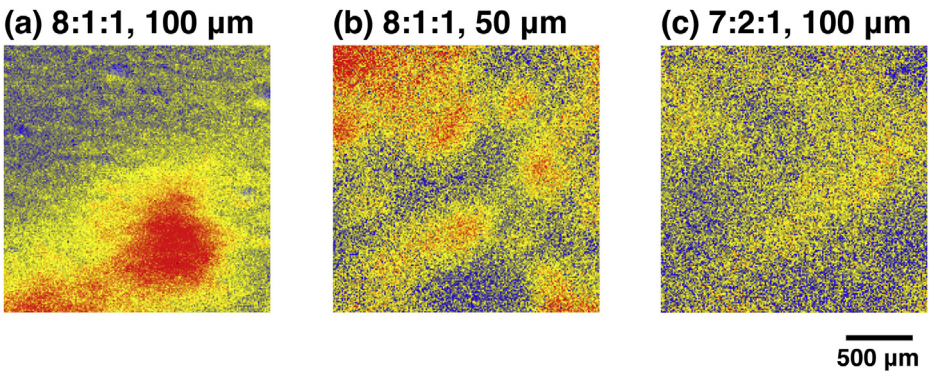

Fig. 4. Comparison of reaction distributions for cathodes fabricated under different preparation conditions. The weight ratios of LFP, acetylene black, and polyvinylidene difluoride and the applied thickness of the cathode mixture are given.

This conclusion is supported by further XAFS imaging of the two cathodes with different compositions and thicknesses. One cathode was prepared with half the previous thickness. The other cathode was prepared with a ratio of cathode materials of 7:2:1 to increase the amount of conductive additive. Fig. 4 shows the chemical state maps obtained at a charging depth of 50%. The number of reaction channels increased for the thinner cathode as shown in Fig. 4(b), because the shorter electron pathways increased the generation possibility of reaction channels. Increasing the amount of conductive additive makes the reaction distribution more uniform (Fig. 4(c)). The carbon additive contributes to the development of electron pathways.

4. Conclusion

The inhomogeneous reaction distribution of active materials in an LFP cathode of LIB has been demonstrated by using our XAFS imaging technique. The electrode reaction occurs in the reaction channels and expands radially. The inhomogeneous distribution is reproduced and reversed during the charge/discharge cycles. These results suggest that the reaction channels correspond to low-resistance electron pathways through the electrode. This understanding of the reaction distribution can be used to improve battery performance because it affects the lifetime and rate properties of LIBs. It is necessary also to investigate the chemical distribution on micrometer to millimeter scales by XAFS imaging to fill the gap between nanometer-scale scientific research and millimeter-scale industrial applications.

Acknowledgment

The authors gratefully acknowledged the New Energy and Industrial Technology Department Organization (NEDO) for supporting Research & Development Initiative for Scientific Innovation on New Generation Batteries (RISING) Project. The XAFS imaging measurements at KEK have been performed under the approval of the Photon Factory Program Advisory Committee (No. 2012G020).

Appendix A. Supplementary data

Supplementary data related to this article can be found at http://dx.doi.org/10.1016/j.jpowsour.2014.03.066.

References

[1] A. Yamada, S.C. Chung, K. Hinokuma, J. Electrochem. Soc. 148 (2001) A224–A229.
[2] S. Nishimura, M. Nakamura, R. Natsui, A. Yamada, J. Am. Chem. Soc. 132 (2010) 13596–13597.
[3] Y.Q. Qiao, J.P. Tu, X.L. Wang, D. Zhang, J.Y. Xiang, Y.J. Mai, C.D. Gu, J. Power Sources 196 (2011) 7715–7720.
[4] K. Zaghib, A. Guerfi, P. Hovington, A. Vijh, M. Trudeau, A. Mauger, J.B. Goodenough, C.M. Julien, J. Power Sources 232 (2013) 357–369.
[5] M.S. Islam, R. Dominko, C. Masquelier, C. Sirisopanaporn, A.R. Armstrong, P.G. Bruce, J. Mater. Chem. 21 (2011) 9811–9818.
[6] H. Duncan, A. Kondamreddy, P.H.J. Mercier, Y.L. Page, Y. Abu-Lebdeh, M. Couillard, P.S. Whitfield, I.J. Davidson, Chem. Mater. 23 (2011) 5446–5456.
[7] H. Wang, T. Abe, S. Maruyama, Y. Iriyama, Z. Ogumi, K. Yoshikawa, Adv. Mater. 17 (2005) 2857–2860.
[8] Y. Fang, Y. Lv, R. Che, H. Wu, X. Zhang, D. Gu, G. Zheng, D. Zhao, J. Am. Chem. Soc. 135 (2013) 1524–1530.
[9] S.D. Beattie, D. Larcher, M. Morcrette, B. Simon, J.-M. Tarascon, J. Electrochem. Soc. 155 (2008) A158–A163.
[10] S.H. Ng, J. Wang, K. Konstantinov, D. Wexler, S.Y. Chew, Z.P. Guo, H.K. Liu, J. Power Sources 174 (2007) 823–827.
[11] A.K. Padhi, K.S. Nanjundaswamy, J.B. Goodenough, J. Electrochem. Soc. 144 (1997) 1188–1194.
[12] R. Malik, F. Zhou, G. Ceder, Nat. Mater. 10 (2011) 587–590.
[13] G.G. Amatucci, J.M. Tarascon, L.C. Klein, J. Electrochem. Soc. 143 (1996) 1114–1123.
[14] S.L. Bewlay, K. Konstantinov, G.X. Wang, S.X. Dou, H.K. Liu, Mater. Lett. 58 (2004) 1788–1791.
[15] C.H. Mi, X.G. Zhang, X.B. Zhao, H.L. Li, J. Alloys Compd. 424 (2006) 327–333.
[16] S. Yang, P.Y. Zavalij, M.S. Whittingham, Electrochem. Commun. 3 (2001) 505–508.
[17] J.-K. Kim, J.-W. Choi, G.S. Chauhan, J.-H. Ahn, G.-C. Hwang, J.-B. Choi, H.-J. Ahn, Electrochim. Acta 53 (2008) 8258–8264.
[18] J. Ma, B. Li, H. Du, C. Xu, F. Kang, J. Solid State Electrochem. 16 (2012) 1353–1362.
[19] D. Jugović, D. Uskokovi&cacute, J. Power Sources 190 (2009) 538–544.
[20] N.A. Hamid, S. Wennig, S. Hardt, A. Heinzel, C. Schulz, H. Wiggers, J. Power Sources 216 (2012) 76–83.
[21] Y.J. Lee, A.M. Belcher, J. Mater. Chem. 21 (2011) 1033–1039.
[22] Z.C. Shi, A. Attia, W.L. Ye, Q. Wang, Y.X. Li, Y. Yang, Electrochim. Acta 53 (2008) 2665–2673.
[23] M.-H. Lee, J.-Y. Kim, H.-K. Song, Chem. Commun. 46 (2010) 6795–6797.
[24] Z.-R. Chang, H.-J. Lv, H.-W. Tang, H.-J. Li, X.-Z. Yuan, H. Wang, Electrochim. Acta 54 (2009) 4595–4599.
[25] K. Saravanan, P. Balaya, M.V. Reddy, B.V.R. Chowdari, J.J. Vittal, Energy Environ. Sci. 3 (2010) 457–464.
[26] Y. Huang, H. Ren, S. Yin, Y. Wang, Z. Peng, Y. Zhou, J. Power Sources 195 (2010) 610–613.
[27] H.H. Lim, I.C. Jang, S.B. Lee, K. Karthikeyan, V. Aravindan, Y.S. Lee, J. Alloys Compd. 495 (2010) 181–184.
[28] S. Yu, S. Dan, G. Luo, W. Liu, Y. Luo, X. Yu, Y. Fang, J. Solid State Electrochem. 16 (2012) 1675–1681.
[29] M.-S. Song, D.-Y. Kim, Y.-M. Kang, Y.-I. Kim, J.-Y. Lee, H.-S. Kwon, J. Power Sources 180 (2008) 546–552.
[30] D. Arumugam, G. Paruthimal Kalaignan, P. Manisankar, J. Solid State Electrochem. 13 (2009) 301–307.
[31] F. Pan, W.-l. Wang, J. Solid State Electrochem. 16 (2012) 1423–1427.
[32] Y. Orikasa, T. Maeda, Y. Koyama, H. Murayama, K. Fukuda, H. Tanida, H. Arai, E. Matsubara, Y. Uchimoto, Z. Ogumi, J. Am. Chem. Soc. 135 (2013) 5497–5500.
[33] K. Zaghib, J. Shim, A. Guerfi, P. Charest, K.A. Striebel, Electrochem. Solid-State Lett. 8 (2005) A207–A210.
[34] Y.H. Chen, C.W. Wang, G. Liu, X.Y. Song, V.S. Battaglia, A.M. Sastry, J. Electrochem. Soc. 154 (2007) A978–A986.

[35] M.E. Spahr, D. Goers, A. Leone, S. Stallone, E. Grivei, J. Power Sources 196 (2011) 3404–3413.
[36] H. Zheng, R. Yang, G. Liu, X. Song, V.S. Battaglia, J. Phys. Chem. C 116 (2012) 4875–4882.
[37] H. Zheng, J. Li, X. Song, G. Liu, V.S. Battaglia, Electrochim. Acta 71 (2012) 258–265.
[38] J. Liu, M. Kunz, K. Chen, N. Tamura, T.J. Richardson, J. Phys. Chem. Lett. 1 (2010) 2120–2123.
[39] J.B. Leriche, S. Hamelet, J. Shu, M. Morcrette, C. Masquelier, G. Ouvrard, M. Zerrouki, P. Soudan, S. Belin, E. Elkaïm, F. Baudelet, J. Electrochem. Soc. 157 (2010) A606–A610.
[40] G. Ouvrard, M. Zerrouki, P. Soudan, B. Lestriez, C. Masquelier, M. Morcrette, S. Hamelet, S. Belin, A.M. Flank, F. Baudelet, J. Power Sources 229 (2013) 16–21.
[41] M. Katayama, K. Sumiwaka, K. Hayashi, K. Ozutsumi, T. Ohta, Y. Inada, J. Synchrotron Radiat. 19 (2012) 717–721.
[42] X. Yu, Q. Wang, Y. Zhou, H. Li, X.-Q. Yang, K.-W. Nam, S.N. Ehrlich, S. Khalid, Y.S. Meng, Chem. Commun. 48 (2012) 11537–11539.
[43] S.-Y. Chung, J.T. Bloking, Y.-M. Chiang, Nat. Mater. 1 (2002) 123–128.
[44] R. Malik, A. Abdellahi, G. Ceder, J. Electrochem. Soc. 160 (2013) A3179–A3197.
[45] V. Srinivasan, J. Newman, J. Electrochem. Soc. 151 (2004) A1517–A1529.
[46] L. Laffont, C. Delacourt, P. Gibot, M.Y. Wu, P. Kooyman, C. Masquelier, J.M. Tarascon, Chem. Mater. 18 (2006) 5520–5529.
[47] C. Delmas, M. Maccario, L. Croguennec, F.L. Cras, F. Weill, Nat. Mater. 7 (2008) 665–671.
[48] G. Kobayashi, S. Nishimura, M.-S. Park, R. Kanno, M. Yashima, T. Ida, A. Yamada, Adv. Funct. Mater. 19 (2009) 395–403.
[49] Y. Orikasa, T. Maeda, Y. Koyama, H. Murayama, K. Fukuda, H. Tanida, H. Arai, E. Matsubara, Y. Uchimoto, Z. Ogumi, Chem. Mater. 25 (2013) 1032–1039.